Atmospheric
Chemistry
and Physics

Optimizing global CO emission estimates using a four-dimensional variational data assimilation system and surface network observations

P. B. Hooghiemstra[1,2], **M. C. Krol**[1,2,3], **J. F. Meirink**[4], **P. Bergamaschi**[5], **G. R. van der Werf**[6], **P. C. Novelli**[7], **I. Aben**[2,6], **and T. Röckmann**[1]

[1]Institute for Marine and Atmospheric Research Utrecht, The Netherlands
[2]Netherlands Institute for Space Research, Utrecht, The Netherlands
[3]Wageningen University, Wageningen, The Netherlands
[4]Royal Netherlands Meteorological Institute, de Bilt, The Netherlands
[5]Joint Research Centre, Institute for Environment and Sustainability, Ispra, Italy
[6]Faculty of Earth and Life Sciences, Free University, Amsterdam, The Netherlands
[7]National Oceanic and Atmospheric Administration, Climate Monitoring and Diagnostics Laboratory, Boulder, USA

Abstract. We apply a four-dimensional variational (4D-VAR) data assimilation system to optimize carbon monoxide (CO) emissions for 2003 and 2004 and to reduce the uncertainty of emission estimates from individual sources using the chemistry transport model TM5. The system is designed to assimilate large (satellite) datasets, but in the current study only a limited amount of surface network observations from the National Oceanic and Atmospheric Administration Earth System Research Laboratory (NOAA/ESRL) Global Monitoring Division (GMD) is used to test the 4D-VAR system. By design, the system is capable to adjust the emissions in such a way that the posterior simulation reproduces background CO mixing ratios and large-scale pollution events at background stations. Uncertainty reduction up to 60 % in yearly emissions is observed over well-constrained regions and the inferred emissions compare well with recent studies for 2004. However, with the limited amount of data from the surface network, the system becomes data sparse resulting in a large solution space. Sensitivity studies have shown that model uncertainties (e.g., vertical distribution of biomass burning emissions and the OH field) and the prior inventories used, influence the inferred emission estimates. Also, since the observations only constrain total CO emissions, the 4D-VAR system has difficulties in separating anthropogenic and biogenic sources in particular. The inferred emissions are validated with NOAA aircraft data over North America and the agreement is significantly improved from the prior to posterior simulation. Validation with the Measurements Of Pollution In The Troposphere (MOPITT) instrument version 4 (V4) shows a slight improved agreement over the well-constrained Northern Hemisphere and in the tropics (except for the African continent). However, the model simulation with posterior emissions underestimates MOPITT CO total columns on the remote Southern Hemisphere (SH) by about 10 %. This is caused by a reduction in SH CO sources mainly due to surface stations on the high southern latitudes.

1 Introduction

Understanding the budget of carbon monoxide (CO) is important, because by reaction with the radical OH, CO influences the oxidizing capacity of the atmosphere significantly (Logan et al., 1981). Enhanced CO concentrations reduce OH concentrations and this has a feedback on the concentration of methane, the second most important anthropogenic greenhouse gas. CO is also a precursor of tropospheric ozone under high $NO_X (NO + NO_2)$ conditions (Seinfeld and Pandis, 2006). CO is emitted into the atmosphere by incomplete combustion of fossil fuels, biofuels and during biomass burning events. In addition, CO is produced throughout the atmosphere by oxidation of methane and non-methane volatile organic compounds (NMVOCs). The main sink of CO is

the reaction with the OH radical. Deposition of CO on the Earth's surface is a minor sink, accounting for 5–10 % of the total sink strength (Sanhueza et al., 1998; Pétron et al., 2002).

The magnitude of CO emissions from different source categories is not well quantified. In particular, emissions from biomass burning (most importantly forest and savanna fires) carry large uncertainties partly due to the variability of fires in both space and time. In addition, bottom-up inventories like the widely used Global Fire Emission Database (GFED) (van der Werf et al., 2004, 2006, 2010) come with substantial uncertainties due to insufficient knowledge about burned area, fuel load, and emission factors (van der Werf et al., 2006). Uncertainties in biomass burning emission estimates are largest in deforestation regions (e.g. South America and Indonesia) and regions where organic soils burn (e.g. Indonesia and the Boreal region).

One way to better constrain emissions of CO is inverse modeling (Enting, 2002). In short, atmospheric measurements, a chemistry transport model (CTM) and a priori information about the emissions are used to optimize the emission in such a way that the mismatch between simulated and observed CO concentrations is minimized. The a priori emission estimates are taken from bottom-up inventories. Throughout the literature there are basically two inversion methods used for CO inversions: synthesis Bayesian inversions (e.g., Bergamaschi et al., 2000; Kasibhatla et al., 2002; Pétron et al., 2002; Palmer et al., 2003, 2006; Arellano et al., 2004, 2006; Heald et al., 2004; Jones et al., 2009) and adjoint inversions (e.g., Müller and Stavrakou, 2005; Yumimoto and Uno, 2006; Stavrakou and Müller, 2006; Chevallier et al., 2009; Kopacz et al., 2009; Fortems-Cheiney et al., 2009; Tangborn et al., 2009; Kopacz et al., 2010). The synthesis inversion optimizes CO emissions over large geographical regions with a preset CO emission distribution in each region, whereas the adjoint inversion technique is able to derive optimized CO emissions on the grid-scale of the underlying CTM, through an iterative approach used to minimize the mismatch between model and observations. Adjoint inversions reduce the risk of aggregation errors and are in particular suited for assimilation of large observational (satellite) datasets (Meirink et al., 2008b; Bergamaschi et al., 2009).

In the current study we apply a 4D-VAR system for CO based on the earlier work for methane (Meirink et al., 2008a,b; Bergamaschi et al., 2009). Although this system is designed to assimilate large observational datasets, it will be tested in this first study by only assimilating surface observations from a limited number of NOAA stations to optimize monthly mean CO emissions for a period of two years. This approach is followed to obtain a benchmark characterization of the system for future assimilation of satellite data. Firstly, we focus on the capability of the system to estimate annual continental emissions by inspecting the reduction of the prior errors assigned to the sources. The optimized emissions will be validated by comparing model results to independent aircraft data from NOAA and satellite data from the Measure-

ments Of Pollution in The Troposphere (MOPITT) instrument (Deeter et al., 2003, 2007, 2010). Secondly, we will investigate the influence of prior settings and model errors on the inversion results by performing sensitivity studies.

This paper is organized as follows: the 4D-VAR system is described in Sect. 2. Section 3 presents the optimized (posterior) emissions and their uncertainty reduction for 2003 and 2004 as well as a validation with independent aircraft and satellite data. The results are discussed in Sect. 4 and the performance of the 4D-VAR system is further investigated by performing sensitivity studies (Sect. 5). Finally we give conclusions in Sect. 6.

2 Description of the four dimensional variational data assimilation system

The 4D-VAR modeling system for CO is based on the TM5-4DVAR system originally developed for methane (Meirink et al., 2008b; Bergamaschi et al., 2009). Given a set of atmospheric observations y and a chemistry transport model H it is possible to optimize a set of fluxes x (the state vector) using the Bayesian technique (Rodgers, 2000). The a posteriori vector x is found by minimizing the mismatch between the model forward simulation $H(x)$ and the observations (y) weighted by an observation error covariance matrix $\mathbf{R}$, while staying close to a set of a priori fluxes x_b, weighted by the a priori error covariance matrix $\mathbf{B}$. Mathematically this problem can be written as the following minimization problem:

$$\hat{x} = \mathrm{Argmin}\, \mathcal{J}$$
$$\mathcal{J}(x) = \frac{1}{2}(x - x_b)^{\top} \mathbf{B}^{-1}(x - x_b)$$
$$+ \frac{1}{2} \sum_{i=1}^{n} (H_i(x) - y_i)^{\top} \mathbf{R}_i^{-1}(H_i(x) - y_i), \quad (1)$$

where the index i refers to the time step and T is the transpose operator. Observations y_i are assimilated in the 4D-VAR system at time i. The classic Bayesian approach determines the a posteriori solution $\hat{x}$ (Rodgers, 2000):

$$\hat{x} = x_b + \mathbf{K}(\mathbf{H}x - y), \quad (2)$$

with $\mathbf{K} = \mathbf{B}\mathbf{H}^{\top}\left(\mathbf{H}\mathbf{B}\mathbf{H}^{\top} + \mathbf{R}\right)^{-1}$ and $\mathbf{H}$ is the Jacobian matrix corresponding to the CTM H (Arellano et al., 2004). The a posteriori error covariance matrix $\mathbf{A}$ can be written as

$$\mathbf{A} = \left(\mathbf{H}^{\top}\mathbf{R}^{-1}\mathbf{H} + \mathbf{B}^{-1}\right)^{-1}. \quad (3)$$

When the number of state vector variables is large, it is not possible to compute the inverse matrices in the above equations directly. Hence an iterative minimization algorithm is required. The conjugate gradient method (Hestenes and Stiefel, 1952) can be used to minimize the cost function (Eq. 1) if the CTM is linear. In general, the CTM H is nonlinear with respect to the state vector x since the CO

emissions perturb OH concentrations and hence the CO sink term. However, for tropospheric CO, Pétron et al. (2002) have shown that to a reasonable approximation, the system can be linearized by using fixed OH fields. In this case the cost function $\mathcal{J}$ is quadratic and we use the same minimization algorithm as in the European Centre for Medium-Range Weather Forecasts (ECMWF) 4D-VAR (Fisher and Courtier, 1995): the cost function $\mathcal{J}$ is minimized and the leading eigenvalues λ_i and eigenvectors v_i of the Hessian of the cost function are derived. The a posteriori error covariance matrix (Eq. 3) describing the uncertainty in the optimized state vector $\hat{x}$, equals the inverse Hessian of the cost function. Hence, the a posteriori error covariance matrix is approximated by a finite combination of the leading eigenvalues and eigenvectors of the Hessian of the cost function added to the a priori error covariance matrix $\mathbf{B}$ (Fisher and Courtier, 1995):

$$\mathbf{A} \approx \mathbf{B} + \sum_{i=1}^{N} \left(\frac{1}{\lambda_i} - 1 \right) (\mathbf{L}v_i)(\mathbf{L}v_i)^\top, \qquad (4)$$

where $\mathbf{L}$ is the preconditioner explained below. The approximation converges to the true posterior error covariance matrix as the eigenvalues converge to 1 if the number of iterations is large enough. The rate of convergence of the minimization is in general quite slow, but a preconditioner can be used to speed up the convergence rate. Fisher and Courtier (1995) have shown that the matrix $\mathbf{L}$ such that $\mathbf{L}\mathbf{L}^\top = \mathbf{B}$ is a suitable preconditioner when used in this 4D-VAR approach. However, due to the large number of state vector elements, the preconditioner is too large to be stored. The approach of Meirink et al. (2008b) is therefore adopted to reduce the required storage. In our study, we consider the minimum of the cost function reached when the norm of the gradient of the cost function is reduced by 99 %. Typically, less than 30 iterations are needed to achieve this reduction. Although the eigenvalues have not yet converged to 1 by this time, the errors on the scale of a continent seem reasonably converged after a limited number of iterations as shown in Fig. 3.

The chemical transport model H, the prior state x_b with uncertainty $\mathbf{B}$ and the observations y with their uncertainty $\mathbf{R}$ will be described in more detail in the following sections.

2.1 The chemical transport model TM5

The CTM (also called the forward model) used in this study to relate CO emissions to atmospheric CO mixing ratios is the two-way nested chemical transport model TM5 (Krol et al., 2005). TM5 is an offline model driven by 3-hourly meteorological fields (6-hourly for 3-D input fields) from the ECMWF. Here we do not use the full-chemistry TM5 model, but the so-called TM5 CO-only model (svn-version 3197). This model, running on a coarse $6° \times 4°$ horizontal grid with 25 vertical layers in this study, deviates from the full-chemistry version by employing simplified CO-OH chemistry. In order to keep the model linear, a monthly OH climatology is used (Spivakovsky et al., 2000), which

is scaled by a factor 0.92 based on methyl chloroform simulations performed for 2000–2006 (Huijnen et al., 2010). The annual mean OH concentration for 2004 amounts to 1.1×10^6 molecules cm^{-3}. The corresponding tropospheric lifetime of methyl chloroform is 4.8 yr.

2.2 Specification of a priori state

The state vector (x in Eq. 1) consists of the variables to be optimized by the inversion. Here we distinguish between monthly surface CO emissions, monthly varying parameters that scale the chemical production of CO from oxidation of methane and NMVOCs, and the initial 3-D CO mixing ratio field. The emissions are divided in three categories: anthropogenic (combustion of fossil fuels and biofuels), natural sources (direct CO emissions from vegetation and the oceans) and biomass burning (open vegetation fires, both natural and human induced).

The a priori anthropogenic emissions are taken from the Emission Database for Global Atmospheric Research (EDGARv3.2) inventory (Olivier et al., 2000, 2003) compiled for the year 1995. The distribution of natural CO emissions (Houweling et al., 1998) is scaled to emit $115\,\mathrm{Tg\,CO\,yr}^{-1}$ which is well within the range of the estimate by Schade and Crutzen (1999) (50–$170\,\mathrm{Tg\,CO\,yr}^{-1}$). Biomass burning emissions are taken from GFED2 (van der Werf et al., 2006). Biomass burning CO is distributed over the vertical model grid as follows: 20 % is released in the layers 0–100 m, 100–500 m and 500–1000 m. The remaining 40 % is released between 1000–2000 m in accordance to Labonne et al. (2007). The sensitivity of the optimized emissions with respect to the chosen injection height is discussed further in Sect. 5.

The chemical production of CO from oxidation of methane and NMVOCs requires monthly 3-D CO production fields. Constant methane mixing ratios of 1800 parts per billion (ppb) are used throughout the atmosphere. Methane is oxidized by the OH climatology using a temperature dependent reaction rate constant (Seinfeld and Pandis, 2006)

$$k = 2.45 \times 10^{-12} \exp(-1775/T). \qquad (5)$$

The CH_4 to CO conversion yield is taken as unity. We acknowledge the possibility of introducing a bias by neglecting the significant N-S gradient in tropospheric CH_4 and the vertical gradient in stratospheric CH_4. The observed 10 % N-S gradient in tropospheric methane would result in a 10 % gradient in CO produced from methane oxidation. Since in our approach, about $880\,\mathrm{Tg\,CO}$ is produced annually from CH_4 oxidation (Table 2), this leads to an overestimate of $45\,\mathrm{Tg\,CO\,yr}^{-1}$ on the SH and a similar underestimate on the NH. Although such a bias is small compared to the global CO emissions and chemical production, we will improve the CH_4 oxidation scheme in the next version of the 4D-VAR system.

A full-chemistry model run using TM4 (Myriokefalitakis et al., 2008) yields monthly 3-D CO fields produced by

oxidation of biogenic and anthropogenic hydrocarbons including CH_4-CO. The total prior CO source from methane and NMVOCs is scaled to 1600 Tg CO yr^{-1} within the range of values used in the literature (1279–1644 Tg CO yr^{-1}) (e.g., Bergamaschi et al., 2000; Müller and Stavrakou, 2005; Duncan et al., 2007; Kopacz et al., 2010). We construct the monthly NMVOC-CO source by subtracting the monthly CH_4-CO described above from the total fields. The 3-D CH_4-CO and NMVOC-CO fields themselves will not be optimized: instead a monthly scaling factor with unit a priori value is optimized. Hence, for these sources we apply a traditional synthesis inversion in the sense that the prior spatial emission patterns are constant and only the global total magnitude of CH_4-CO and NMVOC-CO is optimized.

A forward model simulation with these a priori emissions has been performed for the years 2002–2005 and daily mean CO mixing ratios have been archived. The a priori initial CO mixing ratio field is taken from this archive and further optimized by including the initial 3-D field in the state vector. This approach has been adopted from previous methane 4D-VAR studies (e.g., Meirink et al., 2008b). Also, when optimizing the initial CO mixing ratio field in this way, a long spin up time is not necessary saving up to 50 % of computertime. The approach outlined here yields similar emission estimates compared to an inversion starting from a posterior field from a previous simulation that is not further optimized.

2.3 Specification of a priori uncertainties

2.3.1 Emissions

The prior emission grid-scale errors are set in such a way that in combination with prior correlations (see below), the prior emission errors aggregated to continental regions are in a realistic range. The prior anthropogenic emission inventory used in this study (EDGAR v3.2) is compiled for the year 1995. Inverting for the years 2003/2004, we expect large emission increments due to rapid economic development, particularly in Asia. Hence we assign large errors to this region. In contrast, for the Western developed world (North America, Europe and Australia) we expect that the 2003/2004 anthropogenic emissions are close or somewhat smaller compared to 1995. Therefore, we apply grid-scale errors of 250 % of the corresponding grid-scale emission for the developing world (Asia, Africa and South America) and 50 % for the Western developed world. With these settings, realistic continental-scale errors are computed for the developing world (65–75 %) and the Western developed world (20–48 %) in the range previously used by Stavrakou and Müller (2006).

The grid-scale prior emission errors for biomass burning and the natural source are set to 250 % of the corresponding grid-scale emission, since both inventories bear large uncertainties. For both source categories this leads to prior continental emission errors in the range of 40–100 % (Table 2).

Emission uncertainties are correlated in time and space resulting in a reduction of the effective number of variables to be optimized. For the three emission categories we use a Gaussian spatial correlation length of 1000 km as in Meirink et al. (2008b). An e-folding temporal correlation length of 9.5 months (0.9 month-to-month correlation) is chosen for anthropogenic emissions. This month-to-month correlation is justified because the prior inventory suggests no seasonal cycle. Due to the variable nature of fires in time, the temporal correlation length for biomass burning emissions is set to 0.62 months (0.2 month-to-month correlation). For natural emissions the temporal correlation length is set to 9.5 months.

2.3.2 Initial concentration field and additional parameters

The grid-scale prior initial concentration error is 5 % of the corresponding prior initial concentration. The initial concentration field is correlated in space by a Gaussian correlation length of 1000 km as in Meirink et al. (2008b). The a priori errors on the monthly scaling factors for CO production from methane and NMVOCs are set to 2 % and 8 %, respectively. The scaling factors are correlated in time with a correlation length of 3 months (0.7 month-to-month correlation). This tight error setting is chosen because the NMVOC-CO source is only 1 state vector element per month whereas the other emission categories have a state vector element for each grid box.

2.4 Atmospheric observations

In this first TM5 CO inversion study, only surface observations from NOAA/ESRL GMD are assimilated in the 4D-VAR system. The NOAA surface network provides CO observations from a globally distributed network of stations (Novelli et al., 1998, 2003). A subset of 31 stations, mainly remote stations and stations at larger distances from continental source regions are used in the inversions. Stations close to source regions as well as other stations for which we expect large model errors due to the coarse model resolution are left out. The selected stations are shown in Fig. 1. The observation error consists of the measurement error and the model error. The measurement error is set to 1.5 ppb (Novelli et al., 1998). We estimate the model error using the same approach as described in Bergamaschi et al. (2010). First, the impact of local emissions on the simulated CO mixing ratio is accounted for by a simple emission model for observations in the boundary layer. Second, to account for sub-grid variability that can not be resolved, the vertical component
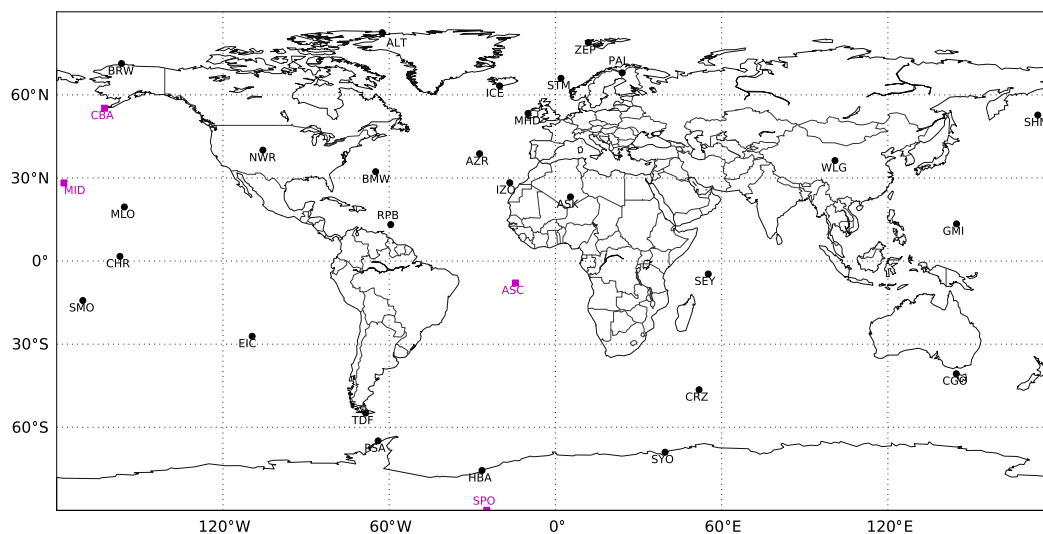
Fig. 1. Positioning of 31 NOAA surface sites (black circles). Purple squares represent stations for which prior and posterior simulations will be shown (Sect. 3.1).

of the model error is calculated from the modeled CO mixing ratios in adjacent grid cells. Third, the temporal standard deviation of the modeled CO mixing ratios within a 3 h window is added to the representation error. With this advanced representation of the model error, we do not account for possible other model uncertainties in vertical transport or the OH field. This will be discussed further in Sects. 4 and 5.

The model error is usually much larger than the measurement error for stations close to or downwind of emission regions (e.g., Fig. 7). In remote areas in the SH, however, the measurement error is the dominant term in the observational error. No correlations between the observations are set resulting in a diagonal observational error covariance matrix **R**.

2.5 Inversion specifics

Although we apply an advanced model error and thus increase the observation error, it is still not expected that the model is capable of simulating all measured pollution events and in particular the transition from polluted to very clean conditions. To account for this and to prevent possible biases due to a few single outliers, the inversion is done in two cycles: after the first inversion we reject all data points that are outside a 3σ error range of the model simulation (Bergamaschi et al., 2010) (see also Fig. 7). Then the second inversion cycle is performed. In the CH$_4$ inversion of Bergamaschi et al. (2010), typically 3 % of the data were rejected, but the a posteriori emissions for both inversion cycles did not differ very much in general. However, in the current study, focusing on the shorter-lived CO, approximately 15–20 % of the data from the first inversion are rejected. Inferred continental emissions in the second cycle are within 15 % of the emissions in the first cycle for most sources/regions and show a

similar pattern of adjustments. The effect of rejecting data on inferred CO emissions will be discussed in more detail in Sect. 4.

The years 2003 and 2004 are inverted separately because the inversions are computationally demanding. The inversions use a one month spin up, in which the emissions are optimized already, but not analyzed, and 2 months spin down to supply enough observations to optimize the emissions in the last months of the year. Given a lifetime of about 2 months for CO, it has been investigated that to optimize emissions of month m, it is sufficient to use observations for months m, $m+1$ and $m+2$ (not shown). Observations at later times will not significantly influence the emissions in month m, because the emission signal is sufficiently diluted and chemically removed by that time. It should be borne in mind, however, that emissions in month m are influenced by emission estimates in surrounding months $(m-3, \ldots, m+3)$ via the prior temporal correlation length.

The length of the state vector is 189 030, that is (15 months $\times$ 3 source categories + 25 vertical layers of the initial concentration field) $\times$ (60 $\times$ 45 grid boxes) + 15 months $\times$ 2 scaling factors. In contrast, the total number of observations is only about 1400 per year. By introducing a non-diagonal prior error covariance matrix, the number of "true" unknowns is greatly reduced to approximately 25 000, but the problem still remains underdetermined (data sparse and hence strongly dependent on a priori knowledge of the emissions). Nevertheless, a grid-scale inversion is performed here to reduce the risk of aggregation errors, which often occur in a big region approach (Stavrakou and Müller, 2006; Meirink et al., 2008b) and to prepare for future ingestion of large amounts of satellite data.
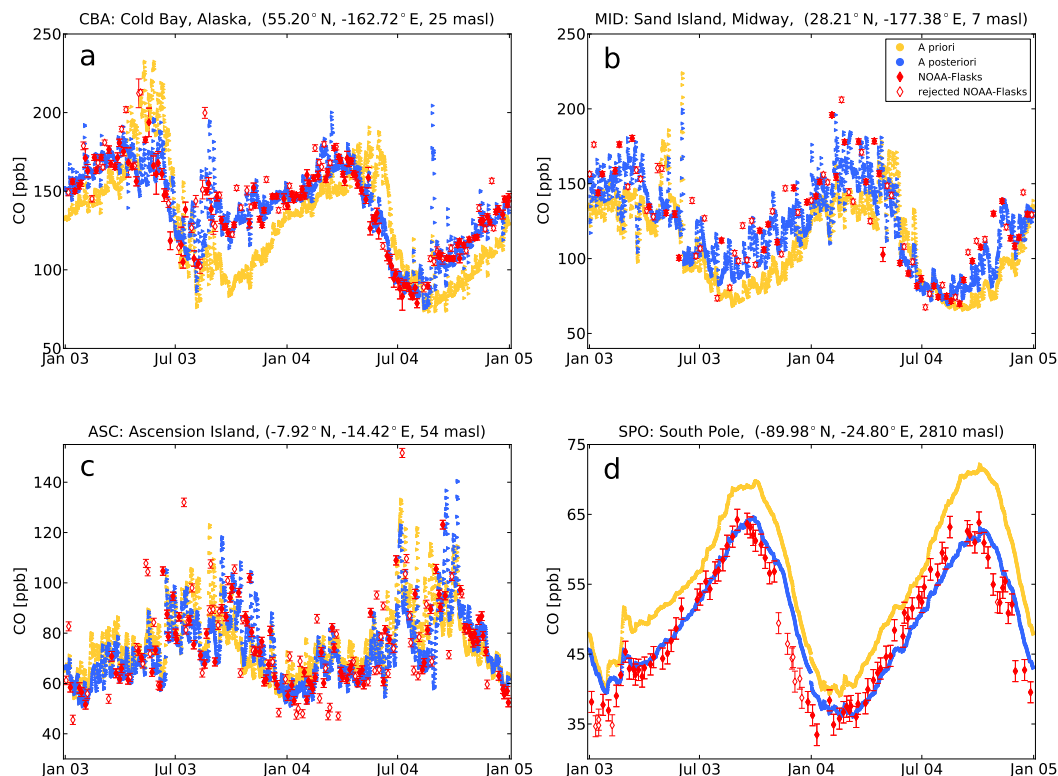
Fig. 2. Comparison of modeled and observed CO mixing ratios at **(a)** Cold Bay, Alaska, **(b)** Sand Island, Midway, **(c)** Ascension Island and **(d)** South Pole station from the NOAA surface network. Red dots correspond to NOAA observations, red open markers represent rejected data from inversion cycle 1 to cycle 2. Model simulations using prior (posterior) settings are shown in yellow (blue).

3 Inversion results

3.1 Comparison of modeled and observed CO mixing ratios

In this section we will discuss the capability of the current 4D-VAR system to adjust the state vector in such a way that background CO mixing ratios as well as observed large scale pollution events are adequately captured. Figure 2 shows the prior and posterior simulation of CO mixing ratios and surface observations for a subset of four stations used in the inversion (purple squares in Fig. 1). All panels show that the model simulation with a priori settings (yellow) is capable to simulate the seasonal cycle and some pollution peaks even though the simulations are performed on a coarse $6° \times 4°$ grid. However, differences with the observations (red) up to 50 ppb are observed. In contrast, the posterior simulation (blue) fits the observations at all four stations rather well. This better fit is obviously caused by combined changes in the surface emissions and in the global source of CO from methane and NMVOCs. A quantitative analysis for all assimilated stations is shown in Table 1 for 2004. Here we present the bias per station for the prior and posterior simulation of the two inversion cycles. A value for the goodness

of fit parameter χ^2/n is also given in this table. A χ^2/n value close to 1 indicates that the system is behaving well.

For station Cold Bay, Alaska (Fig. 2a), representing the high latitude NH, the prior simulation underestimates observed CO mixing ratios up to 50 ppb, in the period September 2003 to February 2004 and from September 2004 to January 2005. For the year 2003, the inversion decreases biomass burning emissions from Russia in spring, but emissions are increased in summer. The posterior annual biomass burning emission estimate for Russia in 2003 is 97 ± 28 Tg CO (compared to the prior estimate of 75 ± 77 Tg CO), well within the range reported by Kasischke et al. (2005) ($55–139$ Tg CO yr^{-1}). This shows that Russian fires account for 60 % of the total CO emissions from biomass burning in Asia in 2003 (158 Tg CO, Table 2). In contrast, in 2004 the inversion increases the Alaskan and Canadian biomass burning emissions in summer, from a prior emission estimate of 16 ± 19 Tg CO from June to August to 36 ± 9 Tg CO as posterior emission estimate. Similar values were also reported by Pfister et al. (2005) and Turquety et al. (2007), and these numbers are in closer correspondence to 30 Tg CO as estimated in the recently released updated GFED (version 3.1, van der Werf et al., 2010). Pfister et al. (2005) inferred CO emissions using satellite observations and reported

Table 1. Statistics of the fit for the stations used in the inversion. Bias is defined as the mean difference between observed (y^o) and modeled (y^m) CO mixing ratio: $\frac{1}{n}\sum_{i=1}^{n}\left(y_i^o - y_i^m\right)$, where n is the number of observations per station and σ_i the observation error for observation y_i^o. The χ^2/n defines the goodness of fit defined as $\frac{1}{n}\sum_{i=1}^{n}\left(\frac{y_i^o - y_i^m}{\sigma_i}\right)^2$. A χ^2/n value close to 1 indicates that the system is behaving well.

| | | | | | Inversion cycle 1 | | | | Inversion cycle 2 | | | |
| | | lat | lon | alt | Bias [ppb] | | χ^2/n | | Bias [ppb] | | χ^2/n | |
ID	station name	[°]	[°]	[m.a.s.l.]	prior	posterior	prior	posterior	prior	posterior	prior	posterior
ALT	Alert, Nunavut, Canada	82.45	−62.52	210.0	0.94	−1.97	6.94	3.01	2.78	0.40	7.29	1.16
ASC	Ascension Island, UK	−7.92	−14.42	54.0	3.20	0.17	5.97	3.03	3.77	−0.34	4.89	1.22
ASK	Assekrem, Algeria	23.18	5.42	2728.0	−3.94	1.21	4.22	1.64	−5.26	−1.14	3.86	0.91
AZR	Terceira Island, Azores, Portugal	38.77	−27.38	40.0	−8.10	−0.86	7.84	4.69	−6.67	−1.01	6.62	1.22
BMW	Tudor Hill, Bermuda, UK	32.27	−64.88	30.0	1.66	−1.06	3.78	1.48	1.98	−2.03	3.11	0.99
BRW	Barrow, Alaska, USA	71.32	−156.60	11.0	−0.52	16.65	6.78	3.05	−1.09	−0.24	6.77	0.91
CBA	Cold Bay, Alaska, USA	55.20	−162.72	25.0	−9.65	0.06	9.04	2.70	−4.33	−0.01	6.96	1.15
CGO	Cape Grim, Tasmania, Australia	−40.68	144.68	94.0	9.18	1.97	1.24	0.37	9.18	2.20	1.24	0.34
CHR	Christmas Island, Republic of Kiribati	1.70	−157.17	3.0	8.79	0.54	4.02	1.58	9.45	0.34	3.86	1.13
CRZ	Crozet Island, France	−46.45	51.85	120.0	5.84	−0.28	3.87	1.14	5.52	−0.20	3.69	0.91
EIC	Easter Island, Chile	−27.15	−109.45	50.0	−9.03	−9.07	5.64	5.26	0.73	−3.07	0.46	1.92
GMI	Mariana Islands, Guam	13.43	144.78	6.0	−8.19	−4.07	4.30	3.23	−1.74	−0.49	2.80	1.32
HBA	Halley station, Antarctica, UK	−75.58	−26.50	33.0	6.93	0.04	4.33	0.65	6.93	0.09	4.33	0.57
ICE	Heimay, Vestmannaeyjar, Iceland	63.25	−20.15	100.0	−0.88	0.97	5.02	1.80	−1.71	−0.22	4.84	1.08
IZO	Izana, Canary Islands, Spain	28.30	−16.48	2360.0	−2.66	−1.45	4.74	2.17	−2.92	−2.66	3.84	1.28
MHD	Mace Head, Ireland	53.33	−9.90	25.0	3.98	2.98	1.60	0.87	4.64	4.02	1.55	0.73
MID	Sand Island, Midway, USA	28.21	−177.38	7.7	−14.07	−0.63	10.26	3.88	−13.81	−0.26	9.74	1.49
MLO	Mauna Loa, Hawaii, USA	19.53	−155.58	3397.0	−3.51	−1.87	3.53	2.47	−0.45	−0.78	2.18	1.28
NWR	Niwot Ridge, Colorado, USA	40.05	−105.58	3526.0	−4.05	2.13	3.13	2.50	−0.88	2.72	2.58	1.22
PAL	Pallas, Finland	67.97	24.12	560.0	−1.88	−3.22	4.08	1.63	−0.19	1.51	3.80	0.81
PSA	Palmer Station, Antarctica, USA	−64.92	−64.00	10.0	6.62	−0.20	3.74	0.63	6.52	0.04	3.74	0.61
RPB	Ragged Point, Barbados	13.17	−59.43	45.0	7.13	0.55	3.85	2.08	7.36	−0.12	3.50	1.13
SEY	Mahe Island, Seychelles	−4.67	55.17	7.0	3.84	0.85	3.41	1.75	5.60	0.75	3.08	0.99
SHM	Shemya Island, Alaska, USA	52.72	174.10	40.0	−7.16	−0.29	9.16	3.24	−2.21	0.77	7.96	1.05
SMO	Cape Matatula, Tutuila, American Samoa	−14.24	−170.57	42.0	4.67	0.28	2.48	1.23	5.06	−0.02	2.36	1.04
SPO	South Pole, Antarctica, USA	−89.98	−24.80	2810.0	6.82	0.50	4.50	1.08	6.60	0.35	4.36	1.01
STM	Ocean station M, Norway	66.00	2.00	5.0	0.36	−0.06	6.67	1.98	1.76	0.23	6.39	1.08
SYO	Syowa Station, Antarctica, Japan	−69.00	39.58	14.0	6.52	0.25	3.81	0.57	6.52	0.17	3.81	0.51
TDF	Tierra del Fuego, La Redonda Isla, Argentina	−54.87	−68.48	20.0	5.89	−0.75	3.73	0.66	5.89	−0.53	3.73	0.60
WLG	Mt. Waliguan, Peoples Republic of China	36.29	100.90	3810.0	−33.31	0.18	19.22	4.27	−21.26	−0.32	13.77	1.03
ZEP	Ny−Alesund, Svalbard, Spitsbergen	78.90	11.88	475.0	1.57	1.76	9.94	3.31	−3.10	0.29	7.69	1.11
ALL					−0.58	0.46	5.54	2.17	1.53	0.21	4.55	1.00

a posterior emission estimate of 30 ± 5 Tg CO. Turquety et al. (2007) constructed a daily biomass burning emission inventory taking into account the emissions from peat burning. They estimated a total of 30 Tg CO from June to August 2004 for North America. Outside the biomass burning season, the inversion attributes increased CO levels to enhanced anthropogenic emissions in East Asia. From Table 1 it is observed that for station Cold Bay the prior bias decreases from −9.7 ppb in the first inversion cycle to −4.3 ppb in the second inversion cycle due to rejection of observations that are not reproduced by the model, likely due to an underestimated model error for this station (see Sect. 4.2). This rejection improves the a posteriori χ^2/n diagnostic for this station from 2.7 to 1.15. The posterior bias is reduced to nearly zero.

For station Sand Island, Midway (Fig. 2b), representing the NH midlatitudes, the prior simulation underestimates observations during the entire period. This is attributed to an underestimation of anthropogenic emissions in the EDGAR inventory, which was compiled for the year 1995. Rapid economic development, particularly in China and India over the last decade led to increased anthropogenic emissions. The posterior simulation shows that increased anthropogenic emissions over China and India (the inversion roughly doubles Asian anthropogenic emissions, see Table 2) results in 15–25 ppb higher CO mixing ratios on stations downwind of South East Asia. Individual observations due to pollution plumes that were not reproduced in the prior simulation are captured better by the model in the posterior simulation. This is due to the fact that the 4D-VAR system computes emission increments on the grid-scale of the underlying chemistry-transport model and hence, better exploits the spatial information present in the measurements. It is acknowledged, however, that a higher spatial model resolution is required to reduce the artificial smearing of concentration gradients.

The tropics are represented here by station Ascension Island (Fig. 2c), and although the improvement from prior to posterior simulation is not clearly visible, Table 1 shows that the posterior bias is nearly zero for both cycles, and the posterior χ^2/n diagnostic is reduced from 3.03 in cycle 1 to 1.22

Table 2. Emissions for 2003 and 2004 per continent for three surface source categories (Anthropogenic, Biomass burning and Natural) and two global chemical production terms (methane and NMVOCs). Per source category, the second and third columns specify the prior emission estimates used, the three right-most columns give the posterior emission estimates for the year 2003 (cycle 2) and 2004 (cycle 1 and cycle 2, respectively). The emissions are given in $Tg\,CO\,yr^{-1}$. Note that the sources of CO production from methane and NMVOC oxidation are given as global totals only, since only a global scaling factor is adjusted. Also, only the biomass burning emission inventory (GFED2) gives year-to-year emissions, the other sources are for the years specified in the footnotes.

Source/Region	Prior		Posterior		
Anthropogenic[a]	2003/2004		2003	2004 cy 1	2004 cy 2
Nam	105 ± 30		85 ± 27	122 ± 27	105 ± 26
Sam	22 ± 16		-9 ± 16	5 ± 16	0 ± 16
Europe	62 ± 30		67 ± 16	94 ± 16	85 ± 18
Africa	80 ± 52		124 ± 48	159 ± 47	149 ± 45
Asia	258 ± 195		497 ± 107	608 ± 97	526 ± 97
Oceania	5 ± 1		5 ± 1	4 ± 1	4 ± 1
Globe	531 ± 183		770 ± 71	993 ± 68	871 ± 77
Biomass burning	2003	2004	2003	2004 cy 1	2004 cy 2
Nam	32 ± 32	23 ± 19	61 ± 30	47 ± 10	47 ± 10
Sam	60 ± 48	98 ± 105	75 ± 37	115 ± 38	136 ± 39
Europe	3 ± 2	2 ± 1	6 ± 2	4 ± 1	3 ± 1
Africa	162 ± 91	165 ± 94	85 ± 72	224 ± 55	165 ± 63
Asia	114 ± 103	98 ± 79	158 ± 54	59 ± 48	42 ± 52
Oceania	24 ± 28	18 ± 14	13 ± 11	34 ± 14	16 ± 14
Globe	397 ± 138	404 ± 157	400 ± 88	482 ± 68	409 ± 76
Natural[b]	2003/2004		2003	2004 cy 1	2004 cy 2
Nam	15 ± 8		12 ± 8	11 ± 8	14 ± 8
Sam	18 ± 13		8 ± 12	28 ± 12	19 ± 12
Europe	4 ± 4		6 ± 4	4 ± 4	5 ± 4
Africa	21 ± 12		29 ± 12	26 ± 12	25 ± 12
Asia	30 ± 12		30 ± 12	33 ± 16	29 ± 11
Oceania	8 ± 6		5 ± 6	6 ± 6	6 ± 6
Globe	115 ± 24		101 ± 24	123 ± 24	111 ± 24
CH4-CO[c]	2003/2004		2003	2004 cy 1	2004 cy 2
Globe	885 ± 10		883 ± 10	893 ± 10	887 ± 10
NMVOC-CO[d]	2003/2004		2003	2004 cy 1	2004 cy 2
Globe	812 ± 40		574 ± 38	301 ± 37	410 ± 38

[a] EDGARv3.2, compiled for the year 1995.

[b] Houweling et al. (1998).

[c] Constant 1800 ppb CH_4.

[d] From a full-chemistry run with TM4 for 2005 Myriokefalitakis et al. (2008). Most important biogenic VOC emissions in this model, isoprene (501 Tg C/yr) and monoterpenes (127 Tg C/yr), are taken from the POET database.

in cycle 2. For the remote SH, represented here by South Pole station (Fig. 2d), the prior simulation overestimates the observations by 5–10 ppb all year long. The inversion attributes this to too high production of CO from NMVOCs since the station is far away from major sources, but neglecting the N-S gradient in tropospheric methane in the model, as discussed before, may also play a role. Again, the posterior bias is nearly zero in both inversion cycles and the χ^2/n diagnostic equals to 1.01 (1.08 in cycle 1).

Overall, Table 1 shows that the inversion reduces prior biases for most of the stations. Although for some stations the posterior bias is slightly larger in cycle 2 compared to cycle 1 (e.g., ASC, AZR, BMW (acronyms are defined in Table 1)), much larger reductions in the bias are observed for other stations (BRW, EIC, GMI). Furthermore, the χ^2/n diagnostic is decreased to approximately 1 in cycle 2 (1.53 in cycle 1). However, for remote stations in the SH, χ^2/n is far smaller than 1 indicating that the measurement error of 1.5 ppb might

be too conservative or indicating the need to take correlations in the observation errors into account. The observation error is further discussed in Sect. 4.2.

3.2 Posterior emission estimates

We present the posterior emission estimates and their uncertainties aggregated over continental scale regions as yearly totals, because the monthly emission estimates on grid-scale level are highly variable as a consequence of the loose prior error settings and the small amount of observations. Also, as shown by Meirink et al. (2008b), the posterior errors converge only rapidly for larger spatial and temporal scales (Fig. 3).

Table 2 and Fig. 3 (blue, solid line) show that on a global scale, a substantial uncertainty reduction of 60 % for the anthropogenic emissions is achieved. In particular Asian anthropogenic emissions are well-constrained by the observations (258 ± 195 Tg CO a priori compared to 497 ± 107 Tg CO in 2003 and 526 ± 97 Tg CO in 2004 a posteriori, see also Fig. 3, dotted blue line). In contrast, African and South American anthropogenic emissions show a negligible uncertainty reduction (Fig. 3, dash-dotted and dashed line respectively). This was expected though, since atmospheric observations mainly constrain the total emissions and the error reduction in those regions is largest for the dominant biomass burning source term. It is acknowledged here, that the presented posterior error reductions are much smaller compared to the study by Kasibhatla et al. (2002). However, the differences are mainly explained by the inversion approach used. Kasibhatla et al. (2002) used a synthesis inversion approach to optimize anthropogenic and biomass burning emissions for a set of big regions. In such a framework, the posterior emission estimates and their errors can be computed by a direct matrix inversion and hence the posterior errors are exact. In the 4D-VAR framework presented here, the cost function is minimized iteratively and considered converged when the norm of the gradient is reduced by a factor 100 (or 99 %). As a special case we continued the iterative proces up to a gradient norm reduction factor of 10^{10}. For this case the approximation of the Hessian of the cost function converged to the true Hessian. The resulting posterior errors are indeed very close to the numbers in Kasibhatla et al. (2002) (not shown). However, a gradient norm reduction factor of 10^{10} is not very practical as the computational burden increases up to a factor 5.

For biomass burning emissions, uncertainty reduction is achieved in South America (98 ± 105 Tg CO a priori compared to 136 ± 39 Tg CO a posteriori in 2004, Fig. 3 red dashed line), Asia (114 ± 103 Tg CO a priori compared to 158 ± 54 Tg CO in 2003) and North America (23 ± 19 Tg CO a priori and 47 ± 10 Tg CO a posteriori in 2004 only). Large changes in biomass burning emissions from 2003 to 2004 are observed for South America and Africa. For South America (with posterior emissions of 75 ± 37 Tg CO in 2003 and
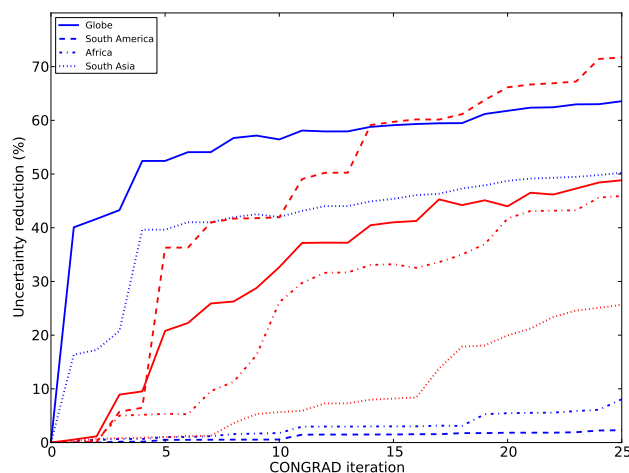
Fig. 3. Uncertainty reduction for 2004, defined as $1 - \frac{\sigma_a}{\sigma_b}$, where $\sigma_a (\sigma_b)$ is the aggregated posterior (prior) uncertainty for the anthropogenic emissions (blue) and biomass burning emissions (red) for four large regions as a function of the iteration number in CONGRAD. A convergence criterium of 99 % gradient norm reduction is used here. The regions are defined as rectangular boxes. For each we give the coordinates of the lower left and the upper right corner. South America: ($-85°$ E,$-60°$ N), ($-30°$ E,$13°$ N). Africa: ($-19°$ E,$-36°$ N), ($51°$ E,$36°$ N). South Asia: ($51°$ E,$-10°$ N), ($180°$ E,$36°$ N).

136 ± 39 Tg CO in 2004) this increment was partly present in the GFED2 prior. Higher emissions in 2004 were also confirmed by observations from the Scanning Imaging Absorption Spectrometer for Atmospheric Cartography (SCIA-MACHY) (Gloudemans et al., 2009) showing the large inter-annual variability in South American biomass burning emissions. In contrast, the posterior biomass burning emission estimates for Africa in 2003 and 2004 seem to compensate for the difference in NMVOC-CO. This is confirmed by the relatively small error reduction and by the study of Chevallier et al. (2009), who optimized African emissions using MO-PITT observations for 2000 to 2006 and did not show large inter annual variability from 2003 to 2004. Table 2 confirms that natural emissions are hardly constrained by the data.

Finally, the uncertainty of the global scaling parameters for the production of CO from methane and NMVOC oxidation is only slightly reduced from the prior to the posterior estimate. This indicates that the current observational dataset does not constrain these individual parameters substantially. However, the value of the scaling factor for the NMVOC-CO (CO from NMVOCs) source is adjusted significantly from a prior global total of 812 ± 40 Tg CO to a posterior global total of 574 ± 38 Tg CO in 2003 and 410 ± 38 Tg CO in 2004. Despite the small prior error, the NMVOC-CO emissions are considerably reduced, far outside the 2σ (95 %) interval, which is mainly due to the overall very small weight of the single monthly NMVOC-CO scaling parameters in the

cost function. Small error settings appeared to be necessary, because the a priori error settings of this global parameter have a strong influence on the solution of the inversion. The optimization approach of NMVOC-CO will be improved in future studies.

3.3 Validation with independent NOAA aircraft observations and MOPITT total columns

We validate our inferred emissions with independent (non-assimilated) aircraft observations from the NOAA aircraft program for 2004. The comparison with aircraft data provides a valuable test for the vertical transport in the model. The NOAA profiles are taken mainly over North America. Figure 4 shows monthly mean deviations (model-observations) for the prior and posterior simulation for aircraft samples at altitudes above 2000 m, thus representing the free troposphere. The prior simulation underestimates the observations throughout the year (except for May and June) probably due to too low anthropogenic emissions in East Asia. The significant overestimation of the prior simulation in May and June is attributed to a too large a priori source of CO from NMVOCs. The posterior simulation matches the observations much better, since the inversion increased Asian anthropogenic emissions and reduced the NMVOC-CO source (Table 2), in particular in May and June (not shown). The uncertainty, given here as a 1σ deviation from the mean, is not reduced significantly from prior to posterior simulation because these observations are not assimilated. Overall, the mean monthly difference is reduced by 50–90 % except for April when deviations were small anyway. The annual mean and standard deviation of the residuals is -6.4 ± 23 ppb a priori and -0.5 ± 22 ppb a posteriori, showing that the inversion is capable to improve the comparison with independent observations in the free troposphere over North America.

We further validate our posterior emissions with CO total column retrievals from MOPITT V4 (level 3, gridded daily profiles, Deeter et al., 2003, 2007, 2010). The MO-PITT instrument is mainly sensitive to free tropospheric CO (4–7 km altitude) and CO at this altitude originates from oxidation of methane or convective transport of surface CO. Figure 5 shows a comparison of observed and modeled CO total columns, where the MOPITT averaging kernels are used to compare properly. Over the well-constrained NH midlatitudes (30° to 60° N), the agreement improves for 2004 from a slight prior underestimate of 5 % to a posterior underestimate of only 1 %. For 2003, the prior underestimate of 5 % turns to a posterior overestimate of 5 %. In the tropics (30° S to 30° N), the comparison improves greatly over the oceans from an a priori model overestimate of 3–5 % to less than 1 % a posteriori in 2004. For 2003 the improvement is smaller. In contrast, over the African continent, the comparison deteriorates from a 3 % underestimate a priori to 6 % a posteriori, probably due to difficulties with the MOPITT retrievals
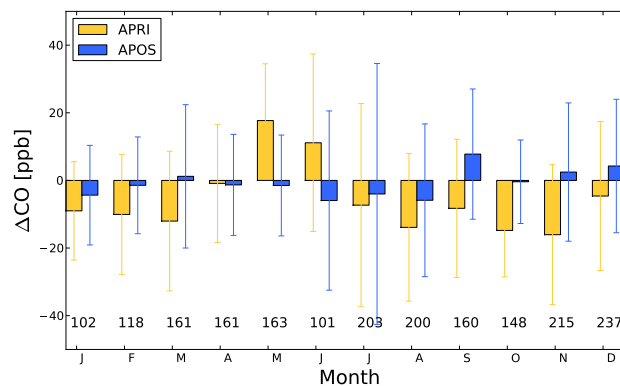
Fig. 4. Monthly mean difference between the TM5 model and NOAA aircraft observations for the prior (yellow) and posterior (blue) simulation. The number of observations per month is also given.

over deserts as observed previously by de Laat et al. (2010). In the remote SH (30° to 60° S), the comparison with MO-PITT deteriorates from a slight model underestimate of 4–6 % a priori to an underestimate of 10 % a posteriori in both years. The prior simulation overestimates surface observations of CO at the remote SH stations (see Fig. 2d). These SH surface observations thus cause a decrease in CO sources (mainly NMVOC-CO) which results in even less CO compared to MOPITT. The model underestimate with respect to MOPITT may be caused by the treatment of vertical transport in the model. For instance, if vertical transport in the model is too slow, CO emissions will remain at low altitudes where the MOPITT instrument is not very sensitive. The comparison with NOAA aircraft profiles suggested however that the vertical transport in TM5 is reasonable, at least over North America. Hence, a possible bias in the MOPITT V4 product as was the case for the previous product MOPITT V3 (Emmons et al., 2009; de Laat et al., 2010) may also play a role. The apparent inconsistency between surface observations and MOPITT CO total columns over the remote SH was (amongst others) also observed by Kopacz et al. (2010). They inverted CO emissions using satellite data only and SH stations used as validation showed a poorer agreement in the posterior simulation compared to the prior.

In conclusion, validating our inversion results with independent aircraft data shows an improved agreement with respect to the prior simulation in the free troposphere even though only surface observations are assimilated. For satellite data, the agreement with MOPITT total column CO improves over the well-constrained NH, but deteriorates in the SH below 30° S.

3.4 Comparison with recent inverse modeling results

The posterior emissions match other recent inverse modeling results for the year 2004 quite well as shown in Table 3.
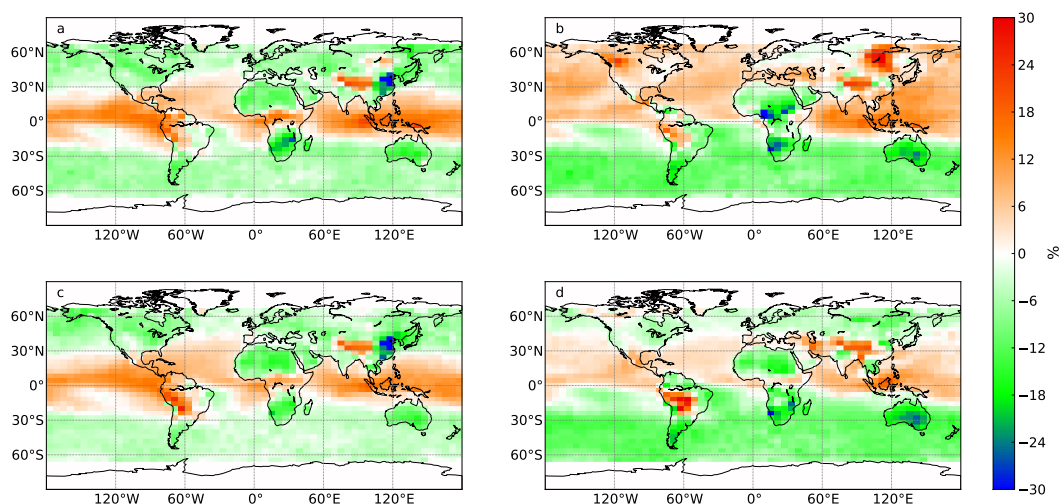
Fig. 5. Annual difference in CO total column, TM5-MOPITT relative to TM5 (%) for the years 2003 (top) and 2004 (bottom). Modeled CO total columns are derived using the prior (left) and posterior (right) emissions. Reddish colors indicate higher TM5 CO total columns compared with MOPITT and greenish colors indicate a lower modeled CO total column compared to MOPITT.

Pison et al. (2009) inverted emissions of CO, methane and H$_2$ simultaneously, using observations from NOAA and updated the OH field within the optimization by assimilating methyl chloroform observations. Results are comparable to our results, but slightly higher for Europe and lower for South America. However, the Australian source of Pison et al. (2009) included CO emissions from Indonesia and is thus significantly higher than in the current study. Kopacz et al. (2010) used satellite data (from MOPITT, the Atmospheric Infrared Sounder (AIRS) instrument and SCIAMACHY) to optimize CO emissions for the period May 2004 to April 2005 and their results showed slightly higher emissions over South America and Asia, but significantly lower emissions over North America. This might be due to their very low prior value for fossil fuel emissions over the United States (35 Tg CO yr^{-1}) based on the US Environmental Protection Agency National Emission Inventory for 1999 (EPA_NEI99). This value was further decreased by 60% following Hudman et al. (2008). In this study we use 105 Tg CO as prior anthropogenic emission over North America. Jones et al. (2009) optimized emissions for November 2004 only, using observations from the MOPITT and TES instruments, and they presented their results as yearly totals. These results are also comparable to the current study except for the Australian source. This is explained by their inclusion of Indonesia into this region. Chevallier et al. (2009) have performed a detailed analysis of African CO emissions for the period 2000–2006. The total emission estimates are by 25% lower than in this study but stay well within the error bounds. The difference with our results is probably explained by the lack of surface data in the tropics. Chevallier et al. (2009) used MOPITT data to constrain the CO emissions and anthropogenic emissions in particular were more constrained than

in the current study. Finally, the large increment in Asian anthropogenic emissions shown in Table 2 also confirms the previous findings of e.g., Kasibhatla et al. (2002) and Arellano et al. (2004) that anthropogenic emissions over Asia are too low in EDGARv3.2. All inversions roughly doubled the Asian emission estimate.

4 Discussion

In our inversions we have used a limited amount of observations from the NOAA surface network. A consequence of solving a data sparse system is a large solution space, because not all degrees of freedom ($\approx 25\,000$) are constrained by the observations (≈ 1400 per year). Thus, the obtained solution will depend on the prior emissions and their error settings. Another consequence might be that model errors are compensated for by emission increments. To investigate these issues, a series of sensitivity studies is presented in Sect. 5. In the following paragraphs we discuss the capability of the system to separate the emission categories and the observation error.

4.1 Separating CO emission categories

In the 4D-VAR setup a mismatch between modeled and observed CO mixing ratios is translated to an adjustment of the prior emissions. However, the observations only constrain total CO emissions of all source categories. The posterior total global source estimates in 2003 and 2004 (1744 ± 76 and 1690 ± 75 Tg CO yr^{-1}, respectively) are rather similar. For individual source categories, large differences are observed from 2003 to 2004. For example, the anthropogenic source increased from 770 ± 71 in 2003 to 871 ± 77 Tg CO yr^{-1}

Table 3. Comparison of prior (left columns) and posterior (right columns) continental emission estimates for 2004 of this study with four recent studies for the same year. Numbers are the sum of anthropogenic, biomass burning and natural emissions given in Tg CO yr^{-1}. Prior inventories and assimilated datasets are given with footnotes.

Region	This study		Pison et al. (2009)[a]		Kopacz et al. (2010)[b]		Jones et al. (2009)[c]		Chevallier et al. (2009)[d]	
	prior	posterior	prior	posterior	prior	posterior	prior	posterior	prior	posterior
Nam	142±37	167±25	137	188	57	71	135	165	–	–
Sam	138±107	156±39	146	131	119	183	113	157	–	–
Europe	67±30	92±17	103	128	78	95	110	111	–	–
Africa	266±108	338±74	264	317	214	343	234	359	286	255
Asia	385±212	597±98	296	539	389	660	367	483	–	–
Oceania	31±15	26±15	96	88	23	41	69	165	–	–
Total	1050 ± 242	1390 ± 89	1042	1391	880	1393	1028	1440	–	–

[a] EDGARv3 (1995) + GFEDv2 combined with flask and continuous surface measurements (56 stations).
[b] EDGAR 3.2FT2000-overwritten with EPA-NEI99 (US), BRAVO (Mexico), EMEP (Europe) and Streets et al. (2006) (Asia/China) + GFEDv2 combined with MOPITT + AIRS + SCIAMACHY retrievals.
[c] Prior emissions from Duncan et al. (2007) combined with MOPITT + TES retrievals.
[d] EDGARv3 + GFEDv2 combined with MOPITT retrievals.

in 2004, whereas the NMVOC-CO source decreased from 574 ± 38 to 410 ± 36 Tg CO yr^{-1}. Although year-to-year variations in the emission estimates is expected, a drop of 150 Tg CO yr^{-1} in the NMVOC-CO source is not physically realistic, but rather an artefact due to the data sparse nature of the current setup.

The prior emission estimates and prior error covariance matrix prescribe the location and timing of the emissions from all source categories. Emissions of sources with a specific timing or spatial pattern prescribed by the prior can be separated. For example, during the dry season (August–November) in the SH, biomass burning is the dominant source of CO, and the system separates the biomass burning source successfully from other CO sources due to its specific timing. In contrast, CO emissions from anthropogenic and NMVOC-CO sources take place throughout the year in the same regions and are therefore difficult to separate. As a consequence, increases of the anthropogenic source are, at least partly, compensated by decreases in the NMVOC-CO source. This may explain the sharp (unphysical) decrease of the NMVOC-CO source from 2003 to 2004, and the increase of the anthropogenic emissions for these years. The interdependence of the anthropogenic and NMVOC-CO source is further illustrated in Fig. 6. The ellipse shows the range of emission estimates for these two sources within 95 % confidence and the tilted axes indicate the negative correlation between them.

Optimizing the NMVOC-CO source by one monthly varying scaling parameter partly caused the compensation between this source and the anthropogenic source. For example, in the remote SH the NMVOC-CO source is the only important source of CO. The prior simulation overestimated the observations in this region, resulting in a decrease of the NMVOC-CO scaling parameter and thus a
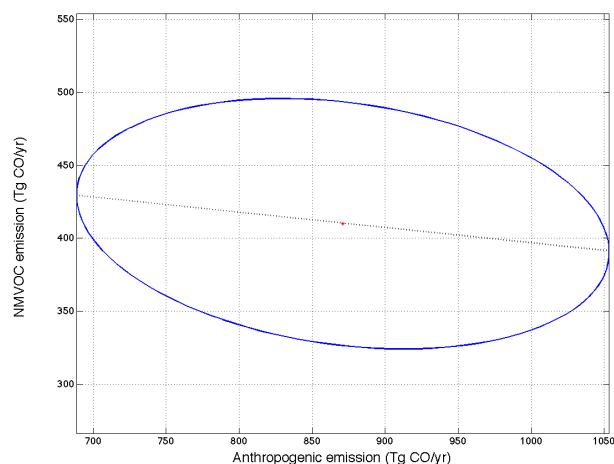

Fig. 6. 95 % confidence ellipse for the global total annual emissions for the anthropogenic and NMVOC-CO source for 2004. The center of the ellipse (red dot) is the posterior emission estimate for the anthropogenic and NMVOC-CO source (871 and 410 Tg CO yr^{-1}, respectively). The emission estimates fall within the ellipse with 95 % confidence. The slightly tilted principle axis of the ellipse is shown as a straight dashed line through the center.

reduced NMVOC-CO source globally. As a consequence, other sources had to be adjusted to compensate for this reduction. However, even with a more advanced optimization approach for the NMVOC-CO source, compensations are expected as the observations only constrain total CO emissions and hence, negative correlations in the posterior emission estimates remain apparent.
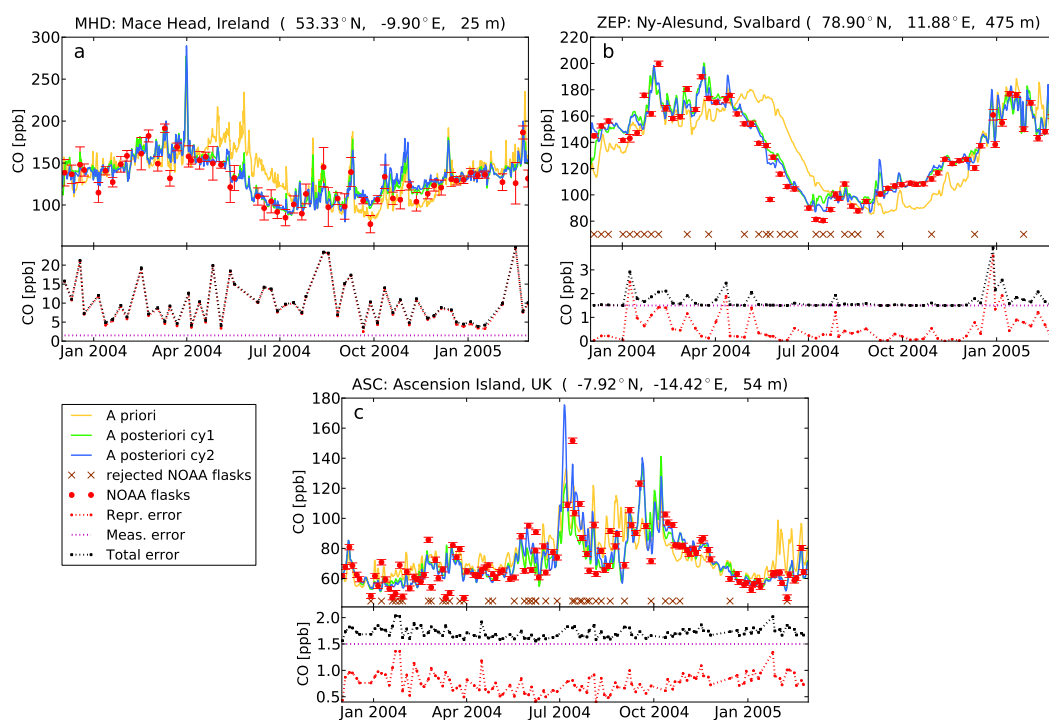
Fig. 7. Top: prior (yellow) and posterior (cycle 1 (green) and cycle 2 (blue)) simulations for **(a)** Mace Head, Ireland, **(b)** Ny-Alesund, Svalbard and **(c)** Ascension Island. The NOAA flasks are shown in red. Rejected observations from cycle 1 to cycle 2 are represented by dark red crosses. Bottom: the observation error is divided in its fixed part (purple) and the model error (red). The total error is shown in black.

4.2 Observation error settings

The inversions in this study are performed in two cycles: after the first cycle, observations that are outside a 3σ interval from the simulated CO mixing ratio, are left out in cycle 2 (Fig. 7). This selection criterion is applied to prevent single outliers to bias the inferred emissions. The number of observations that is left out from cycle 1 to cycle 2 varies largely from station to station: in the SH, on average 6 % of the observations are left out. In the NH, on average 25 % of the observations is left out in cycle 2.

The observation error consists of a measurement error given by Novelli et al. (1998) as 1.5 ppb and a representativeness error as mentioned in Sect. 2.4. This latter contribution varies between 0–20 ppb for most stations. This advanced representation of the observation error has been successfully applied in inversions for methane (Meirink et al., 2008b; Bergamaschi et al., 2010). For the shorter-lived CO, this observation error setting works reasonably for all stations in the remote SH, but only for a few NH stations (e.g., Mace Head, Ireland (MHD), Fig. 7a).

Surprisingly, for the other NH stations (and Ascension Island station located on the SH) the observation error appears rather conservative, and approximately 25 % of the observations are rejected from cycle 1 to cycle 2. This can be at-

tributed either to an underestimation of the measurement error (e.g., station Ny-Alesund, Spitsbergen (ZEP), Fig. 7b) or to an underestimation the representativeness error (e.g., station Ascension Island (ASC), Fig. 7c). Indeed, for station Ny-Alesund located on Spitsbergen, the measurement error of 1.5 ppb is the dominant error term which is clearly too small regarding the number of rejected observations given as red crosses in Fig. 7b. For Ascension Island station the model error (given in red in the bottom panel of Fig. 7c) never exceeds the measurement error even in periods of high CO levels due to pollution peaks transported from continental source regions in either Africa or South America.

The effect of the data rejection strategy on the inferred emissions can be very large both on regional and global scales (Table 2). For example, Asian anthropogenic emissions decrease by $82\,\mathrm{Tg\,CO\,yr^{-1}}$ from cycle 1 to cycle 2, largely driving the $122\,\mathrm{Tg\,CO\,yr^{-1}}$ difference on the global scale. In addition, biomass burning emissions reduce significantly in Africa and Oceania but increase for South America. This behavior shows that measurements are rejected with both very low and very high CO mixing ratios. The global biomass burning source decreases by $73\,\mathrm{Tg\,CO\,yr^{-1}}$ from cycle 1 to cycle 2. In contrast the global NMVOC-CO source increases by $109\,\mathrm{Tg\,CO\,yr^{-1}}$. Given the discussion in the previous paragraph a part of this increase likely compensates

for the drop in anthropogenic emissions. However, the increase in NMVOC-CO alone is not enough to balance the 195 Tg CO yr^{-1} decrease from cycle 1 to cycle 2 for anthropogenic and biomass burning emissions together. Hence, the rejection of observations leads to significant changes in the emissions, even though for most regions the emission estimates remain within 1σ error bounds.

Finally, a sensitivity study with doubled observational errors reduced the number of rejected data points to 7 %. The emission estimates for this simulation also fall within 1σ error bounds of the base run, indicating that the inferred emission estimates are robust given the posterior uncertainties.

We conclude that it is difficult to design an estimation procedure for the model error that gives correct results for all stations, hence estimates of the model representation error will remain a challenging topic for future research.

5 Sensitivity analysis

In this section we discuss 3 sensitivity studies with respect to prior settings and model errors. Sensitivity study GFED3.1 uses the new version of the GFED product (GFEDv3.1, van der Werf et al., 2010). For the year 2004, this biomass burning inventory prescribes lower emissions by a factor 2 to 3 from January to March compared to GFED2. Peak emissions in September in GFED2 of 69 Tg CO month^{-1} globally are reduced to 55 Tg CO month^{-1} in GFED3.1.

Since the distribution of OH and its north-south gradient remains uncertain, we also investigate the influence of the tropospheric OH distribution on the inferred emissions by using an OH field computed from a full-chemistry simulation with TM5 (Huijnen et al., 2010) and scaled by a factor 1.02 to obtain comparable CO and methyl chloroform lifetimes as for the OH field used in the base inversion. Compared to the OH field of the base inversion, the north-south gradient (computed as an airmass-weighted average, Lawrence et al., 2001) in the TM5-OH field is more pronounced (NH/SH ratio of 1.15) compared to the OH field used in the base inversion (NH/SH ratio of 1.0).

The next sensitivity study focuses on model uncertainty in the vertical distribution of biomass burning emissions. The base inversion uses an injection height for biomass burning emissions up to 2000 m (distributed as 20 % in layers 0–100 m, 100–500 m and 500–1000 m and 40 % in 1000–2000 m layer). However, some recent studies (Val Martin et al., 2010; Gonzi and Palmer, 2010) found evidence that biomass burning emissions are partly injected higher up in the atmosphere. In this sensitivity study (FVERT) we apply a vertical distribution of biomass burning emissions following the results of Gonzi and Palmer (2010). The vertical biomass burning emission distribution is defined as

– Boreal region (> 30° N): 82 % below 2 km, 10 % in 2–5 km, 2.5 % in each of the layers 5–8 km and 8–11 km. The remaining 3 % is injected above 11 km.

– Tropical region: 85 % below 2 km, 10 % in 2–5 km, 2.5 % in both layers 5–8 km and 8–11 km.

The inversion results for these sensitivity tests are summarized in Table 4, where we omit the natural emissions and CH4-CO since these sources do not change significantly from the prior to the posterior emission estimates in the base inversion.

5.1 Sensitivity study GFED3.1

The results for sensitivity study GFED3.1 (Table 4) show an increase in biomass burning of 30 Tg CO yr^{-1} globally with respect to the prior estimate of 334 Tg CO yr^{-1}. Biomass burning emissions increase mainly in South America (+45 Tg CO yr^{-1}). However, Asian biomass burning emissions decrease by 17 Tg CO yr^{-1}. To compensate for the lower biomass burning emissions, anthropogenic emissions (932 ± 73 Tg CO) and the NMVOC-CO source (433 Tg CO) are increased with respect to the base inversion. The adjustments in biomass burning emissions were also observed for the base inversion. For example, for the base inversion the increase in South America was 38 Tg CO, whereas Asian biomass burning emissions decreased by 56 Tg CO. This sensitivity study does not support the decrease in global emissions in GFED3.1 compared to GFED2, as emission estimates increase for all regions (except Asia). This could be partly due to the underestimation of agricultural waste burning and deforestation fires in GFED3.1 (van der Werf et al., 2010).

5.2 Sensitivity study OH

The OH field from the TM5 full-chemistry simulation shows lower OH over tropical land masses compared to the OH field from Spivakovsky et al. (2000) (Fig. 8, top), in particular over South America. This OH gap is present since large amounts of emitted isoprene are oxidized by OH and hence reduce OH concentrations in the model. However, as shown by Lelieveld et al. (2008), this OH gap is not confirmed by field campaigns that show high OH over the tropical forests. An OH recycling mechanism was proposed by Lelieveld et al. (2008), but was not yet incorporated in the TM5 simulation (Huijnen et al., 2010). Lower OH concentrations over tropical land masses (Fig. 8, top) result in a reduction of biomass burning emissions of 88 Tg CO yr^{-1} globally in 2004 compared to the base inversion (Table 4, Fig. 8 bottom). Africa (−51 Tg CO yr^{-1}) and South America (−30 Tg CO yr^{-1}) contribute substantially to this decrease. The NMVOC-CO source is reduced to 369 Tg CO yr^{-1}, which is 41 Tg CO yr^{-1} lower than in the base inversion. This reduction is also attributed to the lower OH concentrations in the SH. In contrast, the NH OH concentration is higher compared to the OH field from Spivakovsky et al. (2000). Therefore, higher global anthropogenic emissions are observed for this study (967 Tg CO yr^{-1}) compared to the

Table 4. Prior and posterior global emission estimates (in $Tg\,CO\,yr^{-1}$) for 2004 and their uncertainty for the sensitivity studies. The first column shows the sources/regions. Columns 2 and 3 show the prior (only different for biomass burning in GFED3.1 study). The last 4 columns show the posterior emission estimates for the sensitivity studies. The results for the Base inversion (cycle 2) are included for completeness.

Source/Region	Prior		Posterior			
Anthropogenic	EDGARv3.2		Base	GFED3.1	OH	FVERT
Nam	105 ± 30		105 ± 26	104 ± 27	114 ± 27	82 ± 26
Sam	22 ± 16		0 ± 16	0 ± 16	1 ± 16	0 ± 16
Europe	62 ± 30		85 ± 18	94 ± 18	76 ± 19	73 ± 18
Africa	80 ± 52		149 ± 45	181 ± 50	140 ± 46	178 ± 44
Asia	258 ± 195		526 ± 97	548 ± 99	630 ± 93	512 ± 86
Oceania	5 ± 1		4 ± 1	5 ± 1	4 ± 1	4 ± 1
Globe	531 ± 183		871 ± 77	932 ± 75	967 ± 74	850 ± 69
Biomass burning	GFED2	GFED3.1	Base	GFED3.1	OH	FVERT
Nam	23 ± 19	33 ± 39	47 ± 10	38 ± 7	35 ± 9	58 ± 10
Sam	98 ± 105	64 ± 56	136 ± 39	109 ± 40	106 ± 28	108 ± 31
Europe	2 ± 1	1 ± 1	3 ± 1	1 ± 1	2 ± 1	2 ± 1
Africa	165 ± 94	146 ± 82	165 ± 63	144 ± 44	114 ± 64	214 ± 67
Asia	98 ± 79	69 ± 53	42 ± 52	52 ± 50	42 ± 63	86 ± 50
Oceania	18 ± 14	21 ± 19	16 ± 14	22 ± 18	20 ± 14	16 ± 14
Globe	404 ± 157	334 ± 119	409 ± 76	365 ± 71	321 ± 73	484 ± 76
NMVOC-CO	2004		Base	GFED3.1	OH	FVERT
Globe	812 ± 40		410 ± 38	433 ± 38	369 ± 38	403 ± 38

base inversion ($871\,Tg\,CO\,yr^{-1}$). This difference is clearly observed over India in Fig. 8. The comparison with MOPITT is not improved with respect to the base inversion (not shown): the remote SH still underestimates MOPITT total columns.

5.3 Sensitivity study FVERT

When biomass burning CO emissions are released higher up in the atmosphere, inferred biomass burning emissions are expected to increase, since the surface concentrations of biomass burning CO decrease and thus higher CO surface emissions are required to match the observations. Indeed, it is observed that the global biomass burning emissions increase by $75\,Tg\,CO\,yr^{-1}$ with respect to the base inversion (Table 4). Moreover, this increase is only partly compensated by decreased anthropogenic emissions ($-21\,Tg\,CO\,yr^{-1}$) and a decrease in the NMVOC-CO source ($-7\,Tg\,CO\,yr^{-1}$), indicating that a part of the biomass burning CO emissions released higher in the atmosphere, is not detected by the surface network. Higher biomass burning CO emissions with respect to the base inversion cause the comparison with MOPITT CO total columns to change: over the main biomass burning regions in Africa, South America and South East Asia, the comparison deteriorates, because the base inversion already overestimates MOPITT CO total columns over

these regions (Fig. 5d). On the remote SH, the comparison does not change significantly since the NMVOC-CO source shows only minor changes with respect to the base inversion. We conclude that the biomass burning injection height is a potentially important parameter to take into account in inversions. However, the agreement with MOPITT CO on the SH total columns does not improve. As stated before, it seems that the surface observations and MOPITT CO total columns over the remote SH are not consistently modeled.

6 Conclusions

We have presented a 4D-VAR data assimilation system for CO using simplified chemistry and a fixed OH field, meant to assimilate large satellite datasets, but tested here using surface network observations from NOAA. The posterior simulation reproduces background CO mixing ratios including events with enhanced CO mixing ratios. The mean bias between modeled CO mixing ratios and observations from the NOAA surface network reduces for nearly all stations and the χ^2/n characteristic is reduced to values around 1, indicating that the chosen prior errors result in a well-balanced system. Approximately 15–20 % of the observations is rejected from inversion cycle 1 to cycle 2. This indicates that the model representativeness error requires further improvement. The
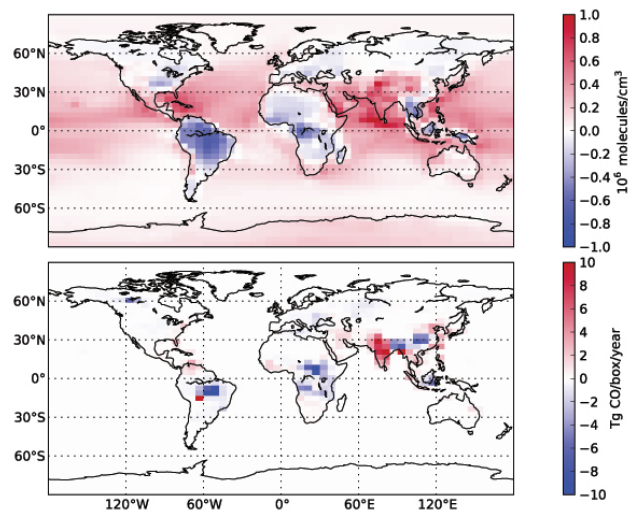
Fig. 8. Top: vertically integrated mass- and rate constant weighted OH difference field (TM5 – Spivakovsky et al., 2000). Bottom: emission increments difference for 2004, OH – Base. Reddish colors indicate higher OH levels in the TM5 OH field compared to the OH field from Spivakovsky et al. (2000) (top) and increased emissions with respect to the base inversion (bottom). Blueish colors indicate lower OH levels (top) and decreasing emissions (bottom).

effect on the inferred emission estimates varies per region. However, for most regions the emission estimates in cycle 1 and cycle 2 are within a 1σ error bound. Uncertainty reductions in the posterior emissions (compared to the prior) up to 60 % on the global scale were observed. For smaller (and less constrained) regions uncertainty reductions varied between 10 and 50 %.

Our annual continental emissions compare well with recent inverse modeling studies, indicating that the global budget of CO is well constrained in our inversion. The posterior emissions have been evaluated against non-assimilated aircraft data from NOAA and vertical column data from MOPITT V4. The forward simulation with the inferred emissions showed much more resemblance with NOAA aircraft observations in the free troposphere compared to the prior simulation, showing that the inversion is capable to improve the free tropospheric CO distribution even though only surface observations are assimilated. The comparison with MOPITT total column CO improves over the well-constrained NH and in the tropics (except over Africa) from the prior to the posterior simulation. However, in the remote SH (30°–60° S), the comparison with MOPITT deteriorates from a 4 % negative bias in the a priori to a 10 % negative bias in the a posteriori solution, due to an emission decrease suggested by SH surface observations.

In general, atmospheric observations only constrain total CO emissions. Since in particular anthropogenic and NMVOC-CO sources are emitted in the same regions and throughout the year, it is difficult to separate these sources.

Hence, emission increments in one source, to compensate for emission changes in another, are observed. However, regions where the timing of the biomass burning emissions is very important (e.g. South America) illustrate the capability to distinguish between anthropogenic and biomass burning emissions. In addition, due to the low spatio-temporal resolution of surface flask observations, the inferred emission estimates are influenced by the emission inventories and model errors. This was investigated by employing a different OH field and a different biomass burning emission height. An OH distribution from a full-chemistry simulation with TM5 with a higher N-S ratio in OH largely influenced the inversion results: biomass burning emissions and NMVOC-CO reduced whereas the anthropogenic emissions increased compared to the base inversion, indicating that the OH distribution over the NH and SH is critical for CO inversions. For this OH field the comparison with MOPITT total column CO in the SH did not improve and even less CO emissions were inferred on the SH. The sensitivity study using different fire injection heights showed that the vertical distribution of biomass burning also largely influences the inversion results. Biomass burning emissions increased by 75 Tg CO yr^{-1} with respect to the base inversion. Again, the comparison with MOPITT total columns did not improve. Increased biomass burning emissions over emission hotspots in South America, Central Africa and Indonesia result in an even larger discrepancy with MOPITT total columns. On the remote SH the comparison with MOPITT was similarly poor as in the base inversion.

The use of satellite data in combination with the network of surface observations is an obvious next step. Assimilation of MOPITT total column CO is expected to lead to more NMVOC-CO on the remote SH, which in turn might reduce biomass burning emissions over the fire hotspots in the SH. Lower biomass burning emissions will be more in line with the new GFED3.1 product. However, surface and satellite observations over the remote SH may bring conflicting information. Therefore, like in the assimilation of SCIAMACHY methane observations (Bergamaschi et al., 2009) a bias correction scheme for satellite data is currently being developed.

Edited by: W. Lahoz

References

Arellano Jr., A. F., Kasibhatla, P., Giglio, L., van der Werf, G., and Randerson, J.: Top-down estimates of global CO sources using MOPITT measurements, Geophys. Res. Lett., 31, L01104, doi:10.1029/2003GL018609, 2004.

Arellano Jr., A. F., Kasibhatla, P., Giglio, L., van der Werf, G., Randerson, J., and Collatz, G.: Time-dependent inversion estimates of global biomass burning CO emissions using Measurement of Pollution in the Troposphere (MOPITT) measurements, J. Geophys. Res., 111, D09303, 10.1029/2005JD006613, 2006.

Bergamaschi, P., Hein, R., Heimann, M., and Crutzen, P. J.: Inverse modeling of the global CO cycle 1. Inversion of CO mixing ratios, J. Geophys. Res., 105, 1909–1927, 2000.

Bergamaschi, P., Frankenberg, C., Meirink, J.-F., Krol, M., G.Villani, Houweling, S., Dentener, F., Dlugokencky, E. J., and Engel, A.: Inverse modeling of global and regional CH4 emissions based on recently revised SCIAMACHY retrievals, J. Geophys. Res., 114, D22301, doi:10.1029/2009JD012287, 2009.

Bergamaschi, P., Krol, M., Meirink, J. F., Dentener, F., Segers, A., van Aardenne, J., Monni, S., Vermeulen, A., Schmidt, M., Ramonet, M., Yver, C., Meinhardt, F., Nisbet, E. G., Fisher, R., O'Doherty, S., and Dlugokencky, E. J.: Inverse modeling of European CH4 emissions 2001–2006, J. Geophys. Res., 115, 4703–4715, 2010.

Chevallier, F., Fortems, A., Bousquet, P., Pison, I., Szopa, S., Devaux, M., and Hauglustaine, D. A.: African CO emissions between years 2000 and 2006 as estimated from MOPITT observations, Biogeosciences, 6, 103–111, doi:10.5194/bg-6-103-2009, 2009.

de Laat, A. T. J., Gloudemans, A. M. S., Aben, I., and Schrijver, H.: Global evaluation of SCIAMACHY and MOPITT carbon monoxide column differences for 2004–2005, J. Geophys. Res., 115, D06307, doi:10.1029/2009JD012698, 2010.

Deeter, M., Emmons, L., Francis, G., Edwards, D., Gille, J., Warner, J., Khattatov, B., Ziskin, D., Lamarque, J.-F., Ho, S.-P., Yudin, V., Attie, J.-L., Packman, D., Chen, J., Mao, D., and Drummond, J.: Operational carbon monoxide retrieval algorithm and selected results for the MOPITT instrument, J. Geophys. Res., 108(D14), 4399, doi:10.1029/2002JD003186, 2003.

Deeter, M. N., Edwards, D. P., and Gille, J. C.: Retrievals of carbon monoxide profiles from MOPITT observations using lognormal a priori statistics, J. Geophys. Res., 112, D11311, doi:10.1029/2006JD007999, 2007.

Deeter, M. N., Edwards, D. P., Gille, J. C., Emmons, L. K., Francis, G., Ho, S.-P., Mao, D., Masters, D., Worden, H., Drummond, J. R., and Novelli, P. C.: The MOPITT version 4 CO product: Algorithm enhancements, validation, and long term stability, J. Geophys. Res., 115, D07306, doi:10.1029/2009JD013005, 2010.

Duncan, B. N., Logan, J. A., Bey, I., Megretskaia, I. A., Yantosca, R. M., Noveli, P. C., Jones, N. B., and Rinsland, C. P.: Global budget of CO, 1988-1997: Source estimates and validation with a global model, J. Geophys. Res., 112, D22301, doi:10.1029/2007JD008459, 2007.

Emmons, L. K., Edwards, D. P., Deeter, M. N., Gille, J. C., Campos, T., Nédélec, P., Novelli, P., and Sachse, G.: Measurements of Pollution In The Troposphere (MOPITT) validation through 2006, Atmos. Chem. Phys., 9, 1795–1803, doi:10.5194/acp-9-1795-2009, 2009.

Enting, I. G.: Inverse Problems in Atmospheric Constituent Transport, Cambridge University Press, Cambridge, 2002.

Fisher, M. and Courtier, P.: Estimating the covariance matrices of analysis and forecast error in variational data assimilation, Tech. rep., ECMWF, Shinfield Park, Reading, 1995.

Fortems-Cheiney, A., Chevallier, F., Pison, I., Bousquet, P., Carouge, C., Clerbaux, C., Coheur, P.-F., George, M., Hurtmans, D., and Szopa, S.: On the capability of IASI measurements to inform about CO surface emissions, Atmos. Chem. Phys., 9, 8735–8743, doi:10.5194/acp-9-8735-2009, 2009.

Gloudemans, A. M. S., de Laat, A. T. J., Schrijver, H., Aben, I., Meirink, J. F., and van der Werf, G. R.: SCIAMACHY CO over land and oceans: 2003–2007 interannual variability, Atmos. Chem. Phys., 9, 3799–3813, doi:10.5194/acp-9-3799-2009, 2009.

Gonzi, S. and Palmer, P. I.: Vertical transport of surface fire emissions observed from space, J. Geophys. Res., 115, D02306, doi:10.1029/2009JD012053, 2010.

Heald, C. L., Jacob, D. J., Jones, D. B. A., Palmer, P. I., Logan, J. A., Streets, D. G., Sachse, G. W., Gille, J. C., Hoffman, R. N., and Nehrkorn, T.: Comparative inverse analysis of satellite (MOPITT) and aircraft (TRACE-P) observations to estimate Asian sources of carbon monoxide, J. Geophys. Res., 109, D23306, doi:10.1029/2004JD005185, 2004.

Hestenes, M. R. and Stiefel, E.: Methods of conjugate gradients for solving linear systems, J. Res. Nat. Bur. Standards, 49, 409–436, 1952.

Houweling, S., Dentener, F., and Lelieveld, J.: The impact of non-methane hydrocarbon compounds on tropospheric photochemistry, J. Geophys. Res., 103, 10673–10696, 1998.

Hudman, R., Murray, L., Jacob, D., Millet, D., Turquety, S., Wu, S., Blake, D., Goldstein, A., Holloway, J., and Sachse, G.: Biogenic versus anthropogenic sources of CO in the United States, Geophys. Res. Lett., 35, L04801, doi:10.1029/2007GL032393, 2008.

Huijnen, V., Williams, J., van Weele, M., van Noije, T., Krol, M., Dentener, F., Segers, A., Houweling, S., Peters, W., de Laat, J., Boersma, F., Bergamaschi, P., van Velthoven, P., Le Sager, P., Eskes, H., Alkemade, F., Scheele, R., Nédélec, P., and Pätz, H.-W.: The global chemistry transport model TM5: description and evaluation of the tropospheric chemistry version 3.0, Geosci. Model Dev., 3, 445–473, doi:10.5194/gmd-3-445-2010, 2010.

Jones, D. B. A., Bowman, K. W., Logan, J. A., Heald, C. L., Liu, J., Luo, M., Worden, J., and Drummond, J.: The zonal structure of tropical O$_3$ and CO as observed by the Tropospheric Emission Spectrometer in November 2004 – Part 1: Inverse modeling of CO emissions, Atmos. Chem. Phys., 9, 3547–3562, doi:10.5194/acp-9-3547-2009, 2009.

Kasibhatla, P., Arellano, A., Logan, J. A., Palmer, P. I., and Novelli, P.: Top-down estimates of a large source of atmospheric carbon monoxide associated with fuel combustion in Asia, Geophys. Res. Lett., 29, 1900, doi:10.1029/2002GL015581, 2002.

Kasischke, E. S., Hyer, E. J., Novelli, P. C., Bruhwiler, L. P., French, N. H. F., Sukhinin, A. I., Hewson, J. H., and Stocks, B. J.: Influences of boreal fire emissions on Northern Hemisphere atmospheric carbon and carbon monoxide, Global Biogeochem. Cy., 19, GB1012, doi:10.1029/2004GB002300, 2005.

Kopacz, M., Jacob, D. J., Henze, D. K., Heald, C. L., Streets, D. G., and Zhang, Q.: Comparison of adjoint and analytical Bayesian inversion methods for constraining Asian

sources of carbon monoxide using satellite (MOPITT) measurements of CO columns, J. Geophys. Res., 114, D04305, doi:10.1029/2007JD009264, 2009.

Kopacz, M., Jacob, D. J., Fisher, J. A., Logan, J. A., Zhang, L., Megretskaia, I. A., Yantosca, R. M., Singh, K., Henze, D. K., Burrows, J. P., Buchwitz, M., Khlystova, I., McMillan, W. W., Gille, J. C., Edwards, D. P., Eldering, A., Thouret, V., and Nedelec, P.: Global estimates of CO sources with high resolution by adjoint inversion of multiple satellite datasets (MOPITT, AIRS, SCIAMACHY, TES), Atmos. Chem. Phys., 10, 855–876, doi:10.5194/acp-10-855-2010, 2010.

Krol, M., Houweling, S., Bregman, B., van den Broek, M., Segers, A., van Velthoven, P., Peters, W., Dentener, F., and Bergamaschi, P.: The two-way nested global chemistry-transport zoom model TM5: algorithm and applications, Atmos. Chem. Phys., 5, 417–432, doi:10.5194/acp-5-417-2005, 2005.

Labonne, M., Bréon, F.-M., and Chevallier, F.: Injection height of biomass burning aerosols as seen from a spaceborne lidar, Geophys. Res. Lett., 34, L11806, doi:10.1029/2007GL029311, 2007.

Lawrence, M. G., Jöckel, P., and von Kuhlmann, R.: What does the global mean OH concentration tell us?, Atmos. Chem. Phys., 1, 37–49, doi:10.5194/acp-1-37-2001, 2001.

Lelieveld, J., Butler, T. M., Crowley, J. N., Dillon, T. J., Fischer, H., Ganzeveld, L., Harder, H., Lawrence, M. G., Martinez, M., Taraborrelli, D., and Williams, J.: Atmospheric oxidation capacity sustained by a tropical forest, Nature, 452, 737–740, doi:10.1038/nature06870, 2008.

Logan, J. A., Prather, M. J., Wofsy, S. C., and McElroy, M. B.: Tropospheric chemistry: a global perspective, J. Geophys. Res., 86, 7210–7254, 1981.

Meirink, J.-F., Bergamaschi, P., Frankenberg, C., d'Amelio, M. T. S., Dlugokencky, E. J., Gatti, L. V., Houweling, S., Miller, J. B., Röckmann, T., Villani, M. G., and Krol, M. C.: Four-dimensional variational data assimilation for inverse modelling of atmospheric methane emissions: Analysis of SCIAMACHY observations, J. Geophys. Res., 113, D17301, doi:10.1029/2007JD009740, 2008a.

Meirink, J. F., Bergamaschi, P., and Krol, M. C.: Four-dimensional variational data assimilation for inverse modelling of atmospheric methane emissions: method and comparison with synthesis inversion, Atmos. Chem. Phys., 8, 6341–6353, doi:10.5194/acp-8-6341-2008, 2008b.

Müller, J.-F. and Stavrakou, T.: Inversion of CO and NO_x emissions using the adjoint of the IMAGES model, Atmos. Chem. Phys., 5, 1157–1186, doi:10.5194/acp-5-1157-2005, 2005.

Myriokefalitakis, S., Vrekoussis, M., Tsigaridis, K., Wittrock, F., Richter, A., Brhl, C., Volkamer, R., Burrows, J. P., and Kanakidou, M.: The influence of natural and anthropogenic secondary sources on the glyoxal global distribution, Atmos. Chem. Phys., 8, 4965–4981, doi:10.5194/acp-8-4965-2008, 2008.

Novelli, P. C., Masarie, K. A., and Lang, P. M.: Distributions and recent changes of carbon monoxide in the lower troposphere, J. Geophys. Res., 103, 19015–19033, 1998.

Novelli, P. C., Masarie, K. A., Lang, P. M., Hall, B. D., Myers, R. C., and Elkins, J. W.: Reanalysis of tropospheric CO trends: Effects of the 1997–1998 wildfires, J. Geophys. Res., 108, 4464, doi:10.1029/2002JD003031, 2003.

Olivier, J. G. J., Berdowski, J. J. M., Peters, J. A. H. W., Bakker, J., Visschedijk, A. J. H., and Bloos, J.-P. J.: Applications of

EDGAR. Including a Description of EDGAR V3.0: Reference Database with Trend Data for 1970-1995, RIVM, Bilthoven, NRP report no. 410200 051/RIVM report no. 773301 001, 2000.

Olivier, J. G. J., Peters, J., Granier, C., Pétron, G., Müller, J., and Wallens, S.: Present and future surface emissions of atmospheric compounds, RIVM, Bilthoven, POET report 2, EU project EVK2-1999-00011, 2003.

Palmer, P. I., Jacob, D. J., Jones, D. B. A., Heald, C. L., Yantosca, R. M., and Logan, J. A.: Inverting for emissions of carbon monoxide from Asia using aircraft observations over the western Pacific, J. Geophys. Res., 108, 8828, doi:10.1029/2003JD003397, 2003.

Palmer, P. I., Suntharalingam, P., Jones, D. B. A., Jacob, D. J., Streets, D. G., Fu, Q., Vay, S. A., and Sachse, G. W.: Using CO_2:CO correlations to improve inverse analysis of carbon fluxes, J. Geophys. Res., 111, 1–11, doi:10.1029/2005JD006697, 2006.

Pétron, G., Granier, C., Khattatov, B., Lamarque, J.-F., Yudin, V., Müller, J.-F., and Gille, J.: Inverse modeling of carbon monoxide surface emissions using Climate Monitoring and Diagnostics Laboratory network observations, J. Geophys. Res., 107, 4761, doi:10.1029/2001JD001305, 2002.

Pfister, G., Hess, P. G., Emmons, L. K., Lamarque, J.-F., Wiedinmyer, C., Edwards, D. P., Pétron, G., Gille, J. C., and Sachse, G. W.: Quantifying CO emissions from the 2004 Alaskan wildfires using MOPITT CO data, Geophys. Res. Lett., 32, L11809, doi:10.1029/2005GL022995, 2005.

Pison, I., Bousquet, P., Chevallier, F., Szopa, S., and Hauglustaine, D.: Multi-species inversion of CH_4, CO and H_2 emissions from surface measurements, Atmos. Chem. Phys., 9, 5281–5297, doi:10.5194/acp-9-5281-2009, 2009.

Rodgers, C. D.: Inverse Methods for Atmospheric Sounding, World Sci., London, 2000.

Sanhueza, E., Dong, Y., Scharffe, D., Lobert, J., and Crutzen, P.: Carbon monoxide uptake by temperate forest soils: the effect of leaves and humus layers, Tellus, 50, 51–58, 1998.

Schade, G. and Crutzen, P. J.: CO emissions from degrading plant matter, Tellus, 51(5), 909–918, 1999.

Seinfeld, J. H. and Pandis, S. N.: Atmospheric Chemistry and Physics: From Air Pollution to Climate Change, John Wiley and Sons, Hoboken, New Jersey, USA, 2006.

Spivakovsky, C. M., Logan, J. A., Montzka, S. A., Balkanski, Y. J., Foreman-Fowler, M., Jones, D. B. A., Horowitz, L. W., Fusco, A. C., Brenninkmeijer, C. A. M., Prather, M. J., Wofsy, S. C., and McElroy, M. B.: Three-dimensional climatological distribution of tropospheric OH: Update and evaluation, J. Geophys. Res., 105, 8931–8980, 2000.

Stavrakou, T. and Müller, J.-F.: Grid-based versus big region approach for inverting CO emissions using Measurement of Pollution in the Troposphere (MOPITT) data, J. Geophys. Res., 111, D15304, doi:10.1029/2005JD006896, 2006.

Streets, D. G., Zhang, Q., Wang, L., He, K., Hao, J., Wu, Y., Tang, Y., and Carmichael, G. R.: Revisiting China's CO emissions after the Transport and Chemical Evolution over the Pacific (TRACE- P) mission: Synthesis of inventories, atmospheric modeling, and observations, J. Geophys. Res., 111, D14306, doi:10.1029/2006JD007118, 2006.

Tangborn, A., Stajner, I., Buchwitz, M., Khlystova, I., Pawson, S., Burrows, J., Hudman, R., and Nedelec, P.: Assimilation of

SCIAMACHY total column CO observations: Global and regional analysis of data impact, J. Geophys. Res., 114, D07307, doi:10.1029/2008JD010781, 2009.

Turquety, S., Logan, J. A., Jacob, D. J., Hudman, R. C., Leung, F. Y., Heald, C. L., Yantosca, R. M., Wu, S., Emmons, L. K., Edwards, D. P., and Sachse, G. W.: Inventory of boreal fire emissions for North America in 2004: Importance of peat burning and pyroconvective injection, J. Geophys. Res., 112, D12S03, doi:10.1029/2006JD007281, 2007.

Val Martin, M., Logan, J. A., Kahn, R. A., Leung, F.-Y., Nelson, D. L., and Diner, D. J.: Smoke injection heights from fires in North America: analysis of 5 years of satellite observations, Atmos. Chem. Phys., 10, 1491–1510, doi:10.5194/acp-10-1491-2010, 2010.

van der Werf, G. R., Randerson, J. T., Collatz, G. J., Giglio, L., Kasibhatla, P. S., Arellano, Jr., A. F., Olsen, S. C., and Kasischke, E. S.: Continental-scale partitioning of fire emissions during the 1997 to 2001 El Niño/La Niña period, Science, 303, 73–76, doi:10.1126/science.1090753, 2004.

van der Werf, G. R., Randerson, J. T., Giglio, L., Collatz, G. J., Kasibhatla, P. S., and Arellano Jr., A. F.: Interannual variability in global biomass burning emissions from 1997 to 2004, Atmos. Chem. Phys., 6, 3423–3441, doi:10.5194/acp-6-3423-2006, 2006.

van der Werf, G. R., Randerson, J. T., Giglio, L., Collatz, G. J., Mu, M., Kasibhatla, P. S., Morton, D. C., DeFries, R. S., Jin, Y., and van Leeuwen, T. T.: Global fire emissions and the contribution of deforestation, savanna, forest, agricultural, and peat fires (1997–2009), Atmos. Chem. Phys., 10, 11707–11735, doi:10.5194/acp-10-11707-2010, 2010.

Yumimoto, K. and Uno, I.: Adjoint inverse modeling of CO emissions over Eastern Asia using four-dimensional variational data assimilation, Atmos. Environ., 40, 6836–6845, 2006.